

Quantification of Planar Cortical Magnification with Optimal Transport and Topological Smoothing

Yujian Xiong^a, Negar Jalili Mallak^a, Yanshuai Tu^a, Zhong-Lin Lu^{b,c,d}, Yalin Wang^{a,*}

⁴*School of Computing and Augmented Intelligence,
Arizona State University, Tempe, AZ, USA*

⁶*bDivision of Arts and Sciences, New York University Shanghai, Shanghai, China*

^c*Center for Neural Science and Department of Psychology, New York University, New York, NY, USA*

⁸*dNYU-ECNU Institute of Brain and Cognitive Science at NYU Shanghai, Shanghai, China*

* To be submitted to NeuroImage

Abstract: 203 words

Title: 96 characters

Pages: 42

Figures: 13

Tables: 5

Please address correspondence to:

Dr. Zhong-Lin Lu
Division of Arts and Sciences,
New York University Shanghai, Shanghai, China
Center for Neural Science and Department of Psychology,
New York University, New York, NY, USA
E-mail: zhonglin@nyu.edu

Dr. Yalin Wang
School of Computing and Augmented Intelligence
Arizona State University
P.O. Box 878809
Tempe, AZ 85287, USA
Phone: (480) 965-6871
Fax: (480) 965-2751
E-mail: ylwang@asu.edu

Abstract

The human visual system exhibits non-uniform spatial resolution across the visual field, which is characterized by the cortical magnification factor (CMF) that reflects its anatomical basis. However, current approaches for quantifying CMF using retinotopic maps derived from BOLD functional magnetic resonance imaging (fMRI) are limited by the inherent low signal-to-noise ratio of fMRI data and inaccuracies in the topological relationships of the retinotopic maps. In this study, we introduced a new pipeline to quantify planar CMF from retinotopic maps generated from the population receptive field (pRF) model. The pipeline projected the 3D pRF solutions onto a 2D planar disk, using optimal transport (OT) to preserve local cortical surface areas, and applied topological smoothing to ensure that the resulting retinotopic maps maintain their topology. We then estimated 2D CMF maps from the projected retinotopic maps on the planar disk using the 1-ring patch method. Applying this pipeline to the Human Connectome Project (HCP) 7T dataset, we revealed previously unobserved CMF patterns across the visual field and demonstrated individual differences among the 181 subjects. The pipeline was further validated on the New York University (NYU) 3T dataset, showing reliable and repeatable results. Our study provided new analytical methods and offered novel insights into visual processing.

- ¹⁰ *Keywords:* Visual Cortex, Functional Magnetic Resonance Imaging (fMRI), Cortical Magnification, Retinotopic Mapping, Topological Smoothing, Optimal Transport
-

¹² **1. Introduction**

The mammalian visual cortex contains multiple representations of distinct regions of the visual field (Horton and Hoyt, 1991; Cowey, 1964). Research on retinotopic representation, based on the activity and anatomy of the visual cortex, has generated considerable interest (Sereno et al., 1995; Engel et al., 1997; Swindale et al., 2000; Wernking et al., 2002a; Wandell et al., 2007; Dougherty et al., 2003). In numerous investigations, retinotopic mapping of the human brain has relied on blood oxygen level-dependent (BOLD) functional magnetic resonance imaging (fMRI) (Schneider et al., 1993; Sereno et al., 1995; Tootell et al., 1995; DeYoe et al., 1996; Engel et al., 1994, 1997; Brewer et al., 2005; Dumoulin and Wandell, 2008; Tootell et al., 1998) and employed the population receptive field (pRF) model (Kay et al., 2013, 2018; Waz et al., 2025) to estimate the centers and sizes of the receptive fields for each vertex on the visual cortical surface, as shown in Fig. 1. The results of these analyses have significantly improved our understanding of the human visual system (Schwarzkopf et al., 2011; Wandell and Winawer, 2011; Brewer and Barton, 2014; Michel et al., 2013; Morland et al., 2001; Kammen et al., 2016; Dumoulin and Wandell, 2008; Benson and Winawer, 2018; Lerma-Usabiaga et al., 2020; Lage-Castellanos et al., 2020).

The cortical magnification factor (CMF), a measure of the amount of cortical tissue in the visual cortex that is devoted to processing a given degree of visual field, has been shown to exhibit unique developmental trajectories that are critical to understanding neurological and psychological functionalities (Hazlett et al., 2011; Ecker et al., 2013; Mensen et al., 2017; Palaniyappan et al., 2011; Cheng et al., 2021; Bois et al., 2015; Rimol et al., 2012; Vuoksimaa et al., 2015; Zacharopoulos et al., 2020; Vuoksimaa et al., 2016). Vision scientists have used CMF to investigate many aspects of processing resources in the cortex, including neural connection density, synaptic efficiency, and brain plasticity.

It has been widely used as a metric to quantify the relationship between visual acuity and cortical anatomy (Cowey and Rolls, 1974; Lage-Castellanos et al., 2020; Bordier et al., 2015; Qiu et al., 2006; Duncan and Boynton, 2003; Song et al., 2015; Zeidman et al., 2018; Yu et al., 2017), offering promising insights into perceptual asymmetries such as horizontal-vertical asymmetry (HVA) (Benson et al., 2021; Himmelberg et al., 2021, 2023b,a), differences between specific visual cortical areas (Cowey and Rolls, 1974; Harvey and Dumoulin, 2011;

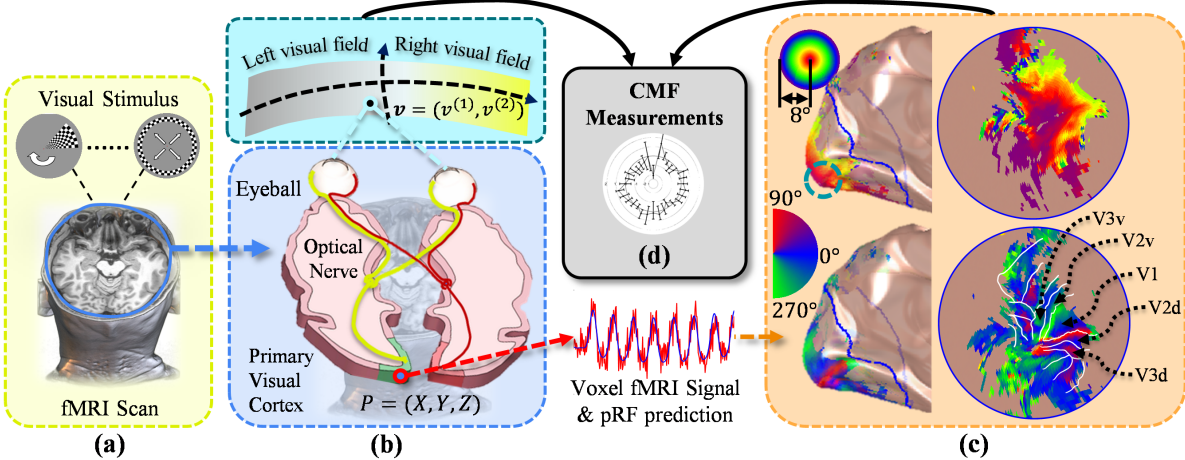


Figure 1: Standard retinotopic mapping through fMRI, pRF modeling and CMF measurements:
 (a) Typical experimental setting with pRF visual stimuli including rotating wedges, expanding rings, and moving bars with checkerboard patterns. (b) These stimuli systematically activate the visual field and its cortical representation in the primary visual cortex. (c) vertex-level BOLD fMRI signals are modeled with the pRF method to estimate receptive field locations; the results are projected onto the cortical surface mesh, displaying eccentricity and polar angle for each surface vertex with labeled anatomical references for vertical and horizontal meridians. (d) Using the surface-based pRF parameters, we could measure 1D CMF (on certain vertical or horizontal directions) or 2D CMF (see Fig. 2).

⁴² Silva et al., 2018; Kupers et al., 2022) and individual differences (Himmelberg et al., 2022; Kupers et al., 2022; Song et al., 2022; Benson et al., 2021; Himmelberg et al., 2021).

⁴⁴ Despite its widespread adoption (Virsu and Hari, 1996; Horton and Hoyt, 1991; Duncan and Boynton, 2003; Song et al., 2015; Hussain et al., 2015; Bordier et al., 2015; Lage-

⁴⁶ Castellanos et al., 2020; Benson et al., 2021; Himmelberg et al., 2021, 2023b,a), traditional approaches for estimating CMF faced notable limitations in both precision and scalability.

⁴⁸ Broadly, two primary approaches have been employed. The first was a model-based method, in which a 2D angle-preserving algebraic model or its enhanced non-conformal variant was

⁵⁰ fitted to the retinotopic maps. CMF was then derived as a function of eccentricity and polar angle from the best-fitting model (Daniel and Whitteridge, 1961; Schwartz, 1977, 1980;

⁵² Schira et al., 2007, 2009). However, studies have found that human retinotopic maps were quasiconformal (Ta et al., 2022). The log-transformation function (Schwartz, 1977, 1980),

⁵⁴ along with its enhanced version incorporating a double-sech shearing function (Schira et al.,

2007), can only approximate the average shape of the retinotopic maps. These models cannot
56 account for asymmetries and local variations among observers, and therefore, they cannot
be used to accurately reconstruct the original retinotopic maps. As a result, they can lead
58 to significant inaccuracies in CMF estimates.

As an alternative to model-based methods, data-driven empirical approaches have gained
60 popularity due to the limitations in precision and generalizability of the former. In the em-
pirical estimation of CMF, a short line was delineated on the cortical surface, and the cor-
62 responding segment was identified in the visual field. The CMF was then calculated as the
ratio between the cortical distance and the corresponding distance in visual space (Cowey
64 and Rolls, 1974). The process typically involved two key steps: (1) extracting the popu-
lation receptive field for each vertex on the cortical surface, including its center and size,
66 based on vertex-level fMRI signals using the pRF model and numerical estimation tech-
niques (Dumoulin and Wandell, 2008; Lage-Castellanos et al., 2020; Lerma-Usabiaga et al.,
68 2020); and (2) mapping these cortical locations to their respective receptive field centers in
the visual field (Harvey and Dumoulin, 2011). In this process, the cortical distance d (in mil-
70 limeters) between neighboring locations was measured along the cortical surface, while the
corresponding change in visual field location, $\Delta\rho$ (degrees of visual angle), was derived from
72 pRF estimates. The CMF was then calculated as the ratio $c = \frac{d}{\Delta\rho}$ (Harvey and Dumoulin,
2011).

74 However, empirical CMF estimation faced two key challenges. **(1). One Dimensional
CMF Measures.** Existing methods typically computed retinotopic maps on a per-vertex
76 basis, resulting in one-dimensional (1D) CMF measures that did not fully capture the inher-
ently two-dimensional (2D) nature of retinotopy. These 1D measurements, often averaged or
78 computed along a single direction, can only reflect asymmetries by comparing the CMF values
in different orientations (Kupers et al., 2022; Silva et al., 2018). Such an approach lacked
80 detailed spatially specific information, particularly near the fovea, where high-resolution
mapping was most critical. A two-dimensional CMF representation was necessary to over-
82 come this limitation. By providing a spatially continuous mapping of the visual field onto
the cortex, 2D CMF enabled a more nuanced understanding of cortical magnification, espe-
84 cially in high-acuity regions with densely packed receptive fields. However, realizing accurate

2D CMF estimation introduced a second major challenge. **(2). Topological Violations.**
Topological violations occurred when mapping from visual space to cortical surface failed
to preserve local neighborhood relationships, particularly in regions with complex geometry,
such as the fovea. The low signal-to-noise ratio and limited spatial resolution in fMRI often
led to such violations in pRF estimates, distorting the smooth and continuous representations
of the visual space on the cortex (Tu et al., 2021). Consequently, CMF measurements may
become distorted or unreliable (Dumoulin and Wandell, 2008; Benson et al., 2018b; Tu et al.,
2021). To mitigate these issues, several optimization methods have been proposed, including
reliability-based analyses of the size of the perceptual field (Lage-Castellanos et al., 2020;
Lerma-Usabiaga et al., 2020), model-free back projections to recover perceptual shapes more
accurately (Merkel et al., 2018, 2020; Lerma-Usabiaga et al., 2021), and various smoothing
techniques such as Gaussian (Warnking et al., 2002b; Bordier et al., 2015), Laplacian (Zei-
dman et al., 2018), and mesh-spectrum-based smoothing (Qiu et al., 2006). While these
techniques improved the robustness of pRF-derived maps, none directly resolve topological
violations — except for our prior work (Ta et al., 2014; Tu et al., 2021; Ta et al., 2022).
Such violations remained a significant barrier to accurate CMF measurements, particularly
on highly curved cortical surfaces (Ta et al., 2022; Tu et al., 2021).

To address the challenges in CMF estimation, we proposed a novel pipeline that applied
optimal transport (OT) (Bonneau, 2013) and topology-preserving smoothing (Tu et al.,
2021) to the retinotopic maps derived from the pRF model. As a mathematical optimization
technique, OT identified the most efficient way to “transport” quantities between specific
locations on two surfaces and can be used to generate area-preserving surface mapping.
Expanding upon our previous research efforts (Su et al., 2015a; Shi and Wang, 2020), where
we successfully relocated individual vertices on a 3D surface onto a 2D planar disk, we
extended this approach to obtain an area-preserving parameterized disk from the cortical
surface. With these techniques, our topology-preserving smoothing algorithm ensured that
the geometric relationships in the retinotopic maps remained intact (Tu et al., 2021, 2022b).
With a topologically correct quantification of retinotopic maps, we can directly compute the
CMF using the 1-ring patch method: for each vertex on the cortical surface, a neighboring
patch is defined and its corresponding “dual patch” was located in the visual field. The areas

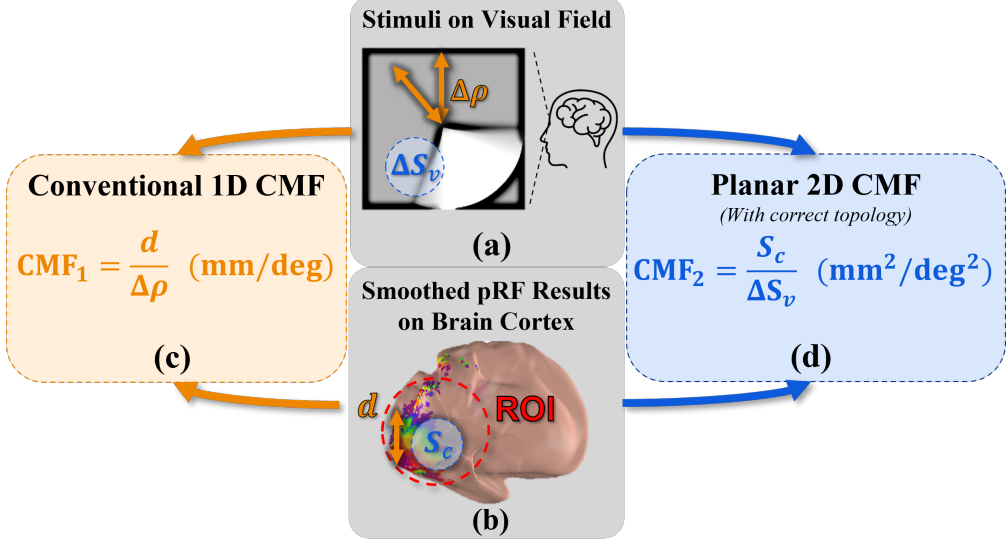


Figure 2: **Comparison of CMF measurements:** (a) The visual field of pRF stimulus viewed by the subjects. (b) The decoded pRF parameters for each vertex on brain cortex, which gives the corresponding receptive center on visual field for vertices. (c) Conventional CMF measurements that approximate CMF by the division between the cortical vertex distance d and visual center distance $\Delta\rho$ on certain vertical or horizontal direction. (d) Our proposed planar CMF measurements that directly calculate the CMF for each vertex through the division between the cortical area S_c of the 1-ring patch around certain vertex and corresponding visual field area ΔS_v . This is only possible when we obtain a topological correct pRF results.

of these dual patches were then used to compute the local 2D CMF value at each vertex.
 116 The key differences between conventional 1D and the proposed 2D CMF measurements are shown in Fig. 2

118 Our pipeline preserved topological structure while enabling detailed quantification of cortical magnification across the visual field. Unlike previous conformal mapping approaches,
 120 our OT-based method improved area correspondence between the cortical surface and the mapped disk, while still preserving both topological and angle relationships. This enhancement
 122 allowed for accurate, region-specific CMF estimation based on area measurements, providing valuable insights into the relationship between cortical magnification and visual
 124 behavior. We validated the effectiveness of our method using real retinotopic data from the Human Connectome Project (HCP) (Benson et al., 2018b) and New York University
 126 (NYU) (Himmelberg et al., 2021). Our results revealed previously undetected CMF patterns across the visual field and highlighted individual differences among subjects.

¹²⁸ **2. Methods and Materials**

2.1. Human Retinotopic Data

¹³⁰ In this study, we used two published human retinotopic datasets.

HCP Dataset. The publicly available retinotopic data from the Human Connectome Project (HCP) can be accessed from (www.humanconnectome.org/study/hcp-young-adult) (Ugurbil et al., 2013; Van Essen et al., 2013) and (<https://osf.io/bw9ec/>) (Benson et al., 2018b) or (<https://balsa.wustl.edu/study/show/9Zkk>) (Van Essen et al., 2017). The current study uses a retinotopic dataset from 181 participants, each of whom underwent retinotopic mapping experiments using 7T fMRI scanning. The dataset includes the fitted pRF results for retinotopy, along with individual cortical surface atlases for each subject.

¹³⁸ *NYU Dataset.* The NYU Retinotopy Dataset (Himmelberg et al., 2021) provides fMRI-based measurements of retinotopic maps in the human visual cortex, including data from ¹⁴⁰ 44 participants. Despite differences in protocols compared to the HCP dataset, the NYU data reliably reproduces key retinotopic properties across visual areas V1, V2, V3, and ¹⁴² hV4. It confirms polar angle asymmetries in cortical magnification and demonstrates strong correlations in population receptive field (pRF) estimates, validating the robustness of fMRI-derived retinotopic maps. This dataset serves as a valuable benchmark for studying visual ¹⁴⁴ area organization and comparing to the HCP 7T Retinotopy Dataset.

¹⁴⁶ *2.2. Retinotopic Mapping*

In this section, we introduce the background and key notations used in the retinotopic mapping experiment. Let the visual stimulus at position $v = (v^{(1)}, v^{(2)})$ be denoted by ¹⁴⁸ $s(t, v)$, where $v^{(1)}$ represents the radial distance from the fovea (i.e., eccentricity) and $v^{(2)}$ represents the polar angle in the visual field. In each retinotopic region of the visual system, ¹⁵⁰ the visual stimulus activates a population of neurons.

¹⁵² The central task of retinotopic mapping is to determine the center v and size $\sigma \in \mathbb{R}^+$ of the perceptual receptive field for each vertex $P = (X, Y, Z) \in \mathbb{R}^3$ on the cortical surface. ¹⁵⁴ BOLD fMRI provides a noninvasive way to obtain the signals needed to estimate v and σ for each point P , following this procedure:

Region Name	Left Hemisphere	Right Hemisphere
V1v	$v^{(2)} = \theta + \pi$	$v^{(2)} = \theta$
V1d	$v^{(2)} = \theta - \pi$	$v^{(2)} = \theta$
V2v	$v^{(2)} = -\theta + 2\pi$	$v^{(2)} = -\theta + \pi$
V2d	$v^{(2)} = -\theta - 2\pi$	$v^{(2)} = -\theta - \pi$
V3v	$v^{(2)} = \theta + 2\pi$	$v^{(2)} = \theta + \pi$
V3d	$v^{(2)} = \theta - 2\pi$	$v^{(2)} = \theta - \pi$

Table 1: Polar angle transformations used to eliminate phase-jumping and correct changes in visual field signs in multiple visual areas (Tu et al., 2021)

- **Stimulus Design:** Design the visual stimulus $s(t; v)$ such that it is uniquely defined by its location, i.e., $s(t; v_1) \neq s(t; v_2), \forall v_1 \neq v_2$;
- **Stimulus Presentation and Data Acquisition:** Present the visual stimuli to a subject and record BOLD fMRI activation $y(t; P)$ at each vertex P on the cortical surface.
- **Population Receptive Field Estimation:** Determine the parameters of the population receptive field model, including the center location v and the size of the receptive field σ , which is most likely to generate the fMRI signal $y(t; P)$ at each cortical vertex P .

The polar angle θ in the visual field's polar coordinate system is discontinuous near the x axis. However, the retinotopic maps are continuous. To remove these phase discontinuities and allow for a unified treatment of the retinotopic maps of the V1-V3 computation, we applied the polar angle transformations developed in our prior work (Tu et al., 2021). These transformations (summarized in Table 1) generated extended polar angles, thereby providing a continuous mapping of retinotopic information across V1, V2, and V3.

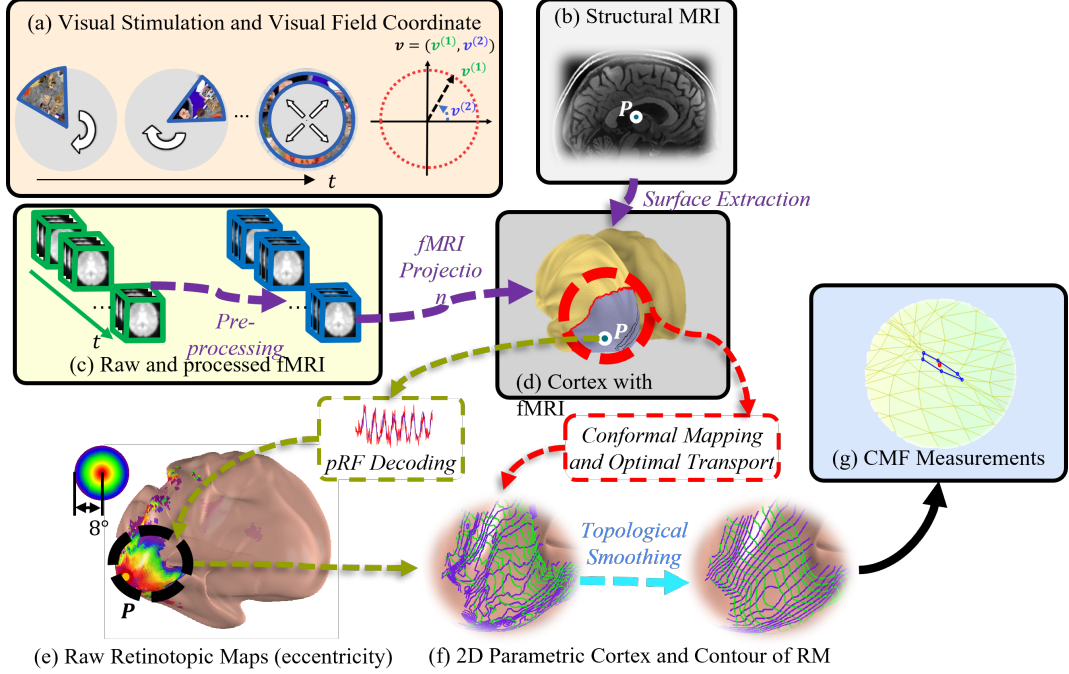


Figure 3: **Overview of pipeline:** Our proposed pipeline began with two primary data inputs: (a) visual stimuli and its coordinate system for the visual field, and (b) structural (anatomical) MR images, along with (c) BOLD fMRI scans. These data underwent preprocessing (c) to prepare them for analysis. Next, we reconstructed the cortical surface and projected the fMRI activation onto this surface (d). Using the population receptive field (pRF) model, we calculated retinotopic maps, extracting the receptive field center and size (σ) for each cortical vertex (e). We then applied the optimal transport to project the cortical surface onto a 2D planar disk, allowing us to visualize clear retinotopic maps and their contours (f). Finally, topology-preserving smoothing was applied to refine the retinotopic maps (f), enabling accurate CMF measurements (g).

2.3. The Pipeline

172 2.3.1. Overview

The pipeline is illustrated in Fig. 3. It began with fMRI pre-processing and projections
 174 onto the cortical surface, followed by the application of area-preserving optimal transport
 (OT) to project the cortical surface onto a flattened 2D surface. Simultaneously, we com-
 176 puted raw retinotopic maps through pRF decoding and apply topology-preserving smoothing
 to correct any topological violations in the retinotopic maps. The smoothed retinotopic maps
 178 were then used for planar CMF computations with the 1-ring patch method. Finally, we
 merged the CMF maps from the two hemispheres to visualize CMF properties and assessed

180 individual differences. This pipeline was applied to both the HCP and NYU datasets.

2.3.2. fMRI Pre-Processing

182 The primary goal of fMRI pre-processing was to accurately capture the brain's time
series of activation in response to visual stimuli, ensuring that the process is both robust
184 and sensitive. To achieve this, we employed the standardized HCP preprocessing pipeline.
First, the cortical surface was extracted from structural MRI images using FreeSurfer software
186 and resampled. Then, the raw fMRI data from each imaging session were co-registered over
time to correct for head movements and other motion artifacts. Finally, the co-registered
188 fMRI data were projected onto the cortical surface, with spatial smoothing applied along
the cortical surface to enhance signal quality. This process resulted in a resampled cortical
190 surface and fMRI activation time series for each point on the cortical surface.

2.3.3. pRF Decoding

192 The population receptive field (pRF) model (Dumoulin and Wandell, 2008; Kay et al.,
2013) was used to determine the receptive field of each vertex $P = (X, Y, Z) \in \mathbb{R}^3$ on the
194 visual cortical surface, including its center location v and size σ in the visual field. For
readers familiar with the pRF model, the visual coordinates in this study are related to the
196 Cartesian coordinates via the transformation: $x = v^{(1)} \cos v^{(2)}$, $y = v^{(1)} \sin v^{(2)}$.

The pRF model predicts the fMRI signal for each vertex based on the following equation:

$$\hat{y}(v, \sigma, n) = \beta \left(\int r(v'; v, n) s(t, v') dv' \right)^n * h(t) \quad (1)$$

198 where β is the activation level, n is the exponent of the power function, v' is a location in
the visual field and v is the center of the receptive field, $r(v'; v, n)$ is the population receptive
200 field model follows a Gaussian kernel: $r(v'; v, n) = \exp\left(-\frac{(x'-x)^2 + (y'-y)^2}{2\sigma^2}\right)$, and $h(t)$ is the
hemodynamic function.

202 The center of the receptive field v and the size of the population receptive field σ are
estimated by minimizing the least square difference between the predicted fMRI signal $\hat{y}(v, \sigma)$
204 and the measured signal $y(P)$, as shown in the following equation:

$$(v, \sigma, n) = \arg \min_{(v, \sigma, n)} |\hat{y}(v, \sigma) - y(P)|^2 \quad (2)$$

This procedure is iterated across all vertices on the visual cortical surface to generate the
 206 raw retinotopic map. The goodness of fit for each vertex is assessed by calculating the R^2
 value:

$$R^2 = 100(1 - \int (\hat{y} - y)^2 / \int y^2 dt). \quad (3)$$

208 *2.3.4. Optimal Transport*

Optimal transport (OT) is a mathematical framework used to determine the optimal
 210 method to transport the mass from one distribution to another, minimizing the associated
 transportation costs. In this approach, we considered two probability measures, $X(x, \mu)$ and
 212 $Y(y, v)$, which belong to the space of all Borel probability measures on a metric space M ,
 denoted by $P(M)$. A measure-preserving mapping $\pi : X(x, \mu) \rightarrow Y(y, v)$ was considered
 214 optimal if it minimized the total transportation cost, which was determined by a given cost
 function $c : M \times M \rightarrow \mathbb{R}_0^+$. The optimal transport plan was represented by the mapping π .

216 The Wasserstein distance, also known as the Earth Mover's distance, is a metric used to
 quantify the similarity between two probability distributions. It is defined as the minimum
 218 cost of transporting the mass between the two distributions, with the cost being computed
 as the distance increased to the power of p : $c(x, \pi(x)) = d(x, \pi(x))^p$, where $d(x, \pi(x))$
 220 is the distance between the point x and its corresponding point $\pi(x)$ under the optimal
 transport plan π . The 2-D Wasserstein distance is obtained by mapping the probability
 222 measures $X(x, \mu)$ and $Y(y, v)$ to a unit hypersphere using volumetric harmonic maps, $\phi_1 : M \rightarrow S^n$ and $\phi_2 : N \rightarrow S^n$, where S^n represents the canonical space parameterized by
 224 Cartesian coordinates. The empirical measures $X'(x, \mu)$ and $Y'(y, v)$ are then defined on
 the transformed supports $\phi_1(\Omega_X)$ and $\phi_2(\Omega_Y)$, respectively. The optimal transport map $T : X' \rightarrow Y'$ is computed to induce the 2-D Wasserstein distance $W_2(X', Y')$. The Wasserstein
 226 distance is then expressed as a sum over a relatively sparse point set $P(p, v)$, obtained by
 228 discretizing Y' , and the distance between two points is measured as $d^2(m_i, p_j) = ||m_i - p_j||^2$,
 where p_j represents the optimal mapping of the point m_i under the optimal transport plan
 230 π (Tu et al., 2020).

In the context of our pipeline, optimal transport can be used to establish the optimal

232 area-preserving mapping between the original cortical surface and the parameterized planar
233 surface, where each 2D point corresponds to a specific vertex on the cortical surface. Rather
234 than simply using a conventional parametric planar surface derived from conformal mapping,
235 we applied optimal transport to calculate the parametric coordinates of each vertex on the
236 cortical surface to preserve the area and topology of the maps. The output was a modified
237 parametric surface that aligns the retinotopic maps more accurately with much less area
238 distortion, enabling CMF computation based on the division of areas.

2.3.5. Optimal Transport

240 Optimal transport (OT) provides a mathematical framework for determining the most
241 efficient way to move mass from one distribution to another while minimizing the total
242 transportation cost. In this study, two probability measures, $X(x, \mu)$ and $Y(y, v)$, are de-
243 fined on a metric space M belonging to the set of Borel probability measures $P(M)$. A
244 measure-preserving mapping $\pi : X(x, \mu) \rightarrow Y(y, v)$ is considered optimal if it minimizes a
245 transportation cost function $c : M \times M \rightarrow \mathbb{R}_0^+$, such that the total cost $\int c(x, \pi(x)) d\mu(x)$ is
246 minimized. The resulting mapping π is the optimal transport plan.

The Wasserstein distance (also called the Earth Mover’s distance) quantifies the mini-
248 mum cost required to transform one probability distribution into another. It is computed as
249 the minimum of $c(x, \pi(x)) = d(x, \pi(x))^p$, where $d(x, \pi(x))$ represents the distance between x
250 and its transported counterpart under π . To compute this distance efficiently, the distribu-
251 tions are embedded onto a unit hypersphere using volumetric harmonic maps, $\phi_1 : M \rightarrow S^n$
252 and $\phi_2 : N \rightarrow S^n$, where S^n denotes a canonical parameterized space in Cartesian coordi-
253 nates. The empirical measures $X'(x, \mu)$ and $Y'(y, v)$ are defined on the transformed supports
254 $\phi_1(\Omega_X)$ and $\phi_2(\Omega_Y)$, respectively. The optimal transport map $T : X' \rightarrow Y'$ induces the two-
255 dimensional Wasserstein distance $W_2(X', Y')$, which is discretized over a finite point set
256 $P(p, v)$ on the target domain. The squared Euclidean distance $\|m_i - p_j\|^2$ serves as the local
257 transport cost between each pair of source and target points.

258 In our implementation, we adopt the discrete variational OT formulation described by (Tu
259 et al., 2020), which models the mapping as a convex optimization problem. The algorithm
260 iteratively updates a set of vertex weights that define a convex cell decomposition (also

known as a lifted power diagram (Tu et al., 2020; Gu et al., 2016)) until the transported
262 mass between neighboring regions matches their target areas. The gradient of the trans-
port energy guides the adjustment of these weights, while the Hessian matrix of the energy
264 function ensures convergence through Newton’s method (Villani, 2008). This iterative pro-
cess continues until the difference between the source and target areas falls below a small
266 threshold, yielding an area-preserving mapping between the two surfaces (Tu et al., 2020).

Within our pipeline, the OT-based mapping establishes an optimal correspondence be-
268 tween the original cortical surface and a planar parameterization, ensuring that the local
area of each surface element is preserved after flattening. Unlike conformal mappings, which
270 preserve angles but distort areas, the OT mapping minimizes local area distortion while
maintaining global topological consistency. The resulting two-dimensional disk provides a
272 smooth, bijective parameter domain where each cortical vertex corresponds uniquely to a
planar vertex, forming a robust foundation for subsequent topological smoothing and CMF
274 computation.

2.3.6. Topological Smoothing

Topological smoothing (Tu et al., 2021, 2022b) is an iterative optimization procedure de-
276 signed to smooth retinotopic maps while preserving their topological structure. The cortical
surface is represented as a triangular mesh, and each geodesic disk patch is parameterized
278 onto a two-dimensional unit disk using prior area-preserving optimal transportation method.
Within this parametric domain, the retinotopic coordinates (eccentricity and polar angle)
280 are iteratively refined under quasiconformal constraints, measured by the **Beltrami coeffi-**
cient μ , which must satisfy $|\mu| < 1$ for all triangles to ensure a diffeomorphic mapping (Tu
282 et al., 2021).

At each iteration, a new smooth map \hat{v} is generated through three main steps:

1. **Boundary update:** Boundary visual coordinates are fitted by local polynomial re-
gression and restricted within a tolerance t to avoid excessive displacement.
286
2. **Topological correction:** Local orientation flips are detected using the Beltrami coef-
ficient and corrected by averaging boundary vertices within k -nearest neighbors. The
smoothing strength is adaptively increased (i.e., a larger k) until all triangles satisfy
288

290 the topological constraint.

3. **Laplacian smoothing:** The interior vertices are updated by solving the following
292 linear system (Eilers, 2003; Garcia, 2010; Tu et al., 2021):

$$(\text{diag}(R^2) + \lambda\Delta)\hat{v} = \text{diag}(R^2)v,$$

294 where Δ denotes the discrete Laplace-Beltrami operator, R^2 denotes the pRF-decoding
reliability, and λ denotes the smoothness factor.

The iterations continue until convergence, defined by both the topological condition
296 ($|\mu| < 1$) and the stability of vertex updates bounded by the parameter *meanddth*. In
addition, the loop is limited to a maximum of 20 iterations to prevent unbounded smooth-
298 ing. Our parameter choices follow the protocol described in (Tu et al., 2022b) but with
stricter conditions: $t = 0.05$, $\lambda = 0.001$, $k = 3$, and *meanddth* = 1.0. In practice, most
300 subjects satisfied these criteria well before the 20-iteration cap. The resulting map achieves
a strong balance between surface smoothness and faithful preservation of cortical topology.

302 In application to the 181 HCP subjects, the algorithm successfully converged for all
cases within 20 iterations. After smoothing, every subject’s retinotopic map became fully
304 topologically correct, exhibiting zero flipped triangles. The process maintained diffeomorphic
consistency while preserving close agreement with the original pRF decoding results, showing
306 only a minor reduction in the explained variance (R^2) due to the topological constraint (Tu
et al., 2021). Importantly, the method preserves genuine biological discontinuities—such as
308 those potentially arising in clinical or pathological conditions—because topological correction
only targets spurious local flips while maintaining the global organization of the map (Tu
310 et al., 2021).

2.3.7. One-Ring Patch Method

312 The Cortical Magnification Factor (CMF) can be estimated using a local structural
method based on the vertex dual structure over a one-ring patch. The vertex one-ring
314 is defined as the set of immediate neighbors of a center vertex, i.e., all vertices that can be
reached by traversing a single edge. Fig. 4a illustrates a vertex (the central red point) and
316 its associated one-ring patch, represented by the enclosed blue polygon.

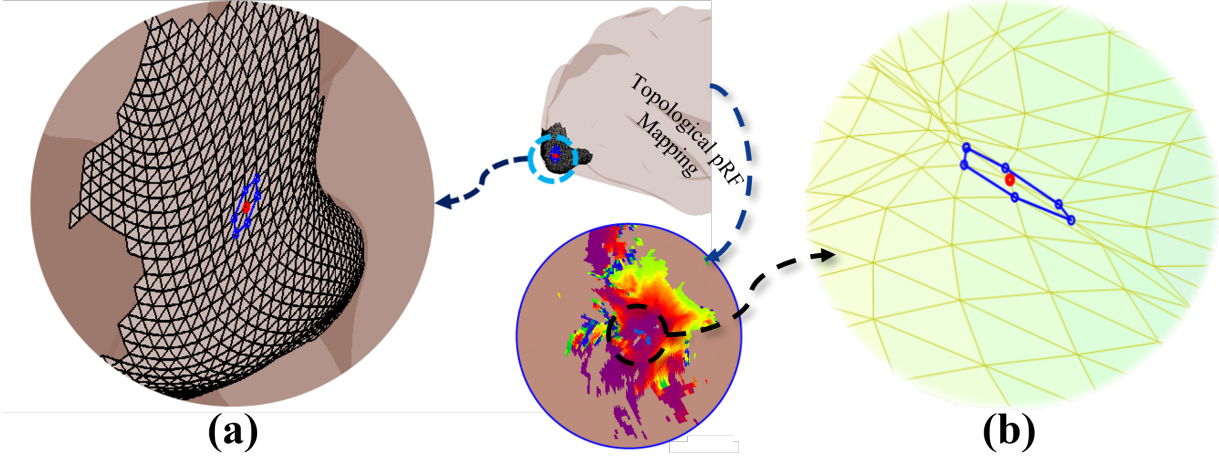


Figure 4: 1-ring patch measurement: estimation of cortical magnification factor by the division between areas of the dual rings. (a) A vertex’s dual ring structure on 3D brain mesh, (b) The dual ring structure on the retina visual space.

After the cortical surface within the V1–V3 complex is topologically smoothed, each vertex on the three-dimensional mesh is assigned a receptive-field location in visual space. This provides a topologically correct retinotopic map in which each cortical vertex corresponds to a unique visual coordinate. For a given vertex v_i , we identify its one-ring neighborhood $\mathcal{N}(v_i)$ on the 3D mesh and compute two quantities: (1) the cortical-surface area, defined as the sum of the face areas enclosed by $\mathcal{N}(v_i)$; and (2) the visual-field area, defined as the polygonal area formed by the mapped receptive field centers $\{v'\}$ in visual space corresponds to $\mathcal{N}(v_i)$ (Fig. 4b). The CMF at vertex v_i is then given by the ratio of these two areas:

$$\text{CMF}(v_i) = \frac{\text{Area}_{\text{cortex}}}{\text{Area}_{\text{visual}}} = \frac{\text{Area}_{\mathcal{N}(v_i)}}{\text{Area}_{\{v'\}}}$$

It is important to emphasize that in our study the CMF 1-ring measurement is always defined between the visual space and the original 3D cortical mesh. The 2D mapping obtained with optimal transport is used only to enable stable topological smoothing and to enforce diffeomorphic constraints during preprocessing. Once the smoothed retinotopic map is obtained, the final CMF estimation is carried out entirely on the 3D surface, consistent with prior approaches (Schira et al., 2007, 2009).

This method relies on topologically accurate retinotopic mapping: non-topological maps

332 can lead to inverted or flipped neighborhood $\{v'\}$ in visual space, generating highly noisy
333 and unreliable CMF estimates. By incorporating topological constraints via optimal trans-
334 port flattening and Beltrami coefficient-based smoothing, our pipeline ensures robust and
physiologically consistent results.

336 Finally, the CMF results from the left and right hemispheres were merged to provide a
unified representation of the perceptual resource distribution across the visual field.

338 *2.3.8. Merge Per-Hemisphere CMF to Entire Visual Field*

340 Because fMRI measurements provide cortical surface reconstructions for the left and
342 right hemispheres separately, the $CMF(v_i)$ values were first computed for each hemisphere
independently. To obtain a unified representation of cortical magnification across the entire
344 visual field and to illustrate individual patterns of visual concentration, the results from the
two hemispheric were merged onto a common two-dimensional coordinate system, as shown
in Fig. 5.

346 Specifically, the CMF values for each hemisphere were projected from their cortical sur-
348 face vertices to the corresponding receptive-field centers in visual-field coordinates (ρ, θ) ,
where ρ denotes eccentricity and θ denotes polar angle. A uniform 100×100 grid was de-
350 fined over the visual field to serve as the reference domain. For each grid location, CMF
values were interpolated from the nearest cortical-vertex measurements, with separate passes
352 for the left and right hemispheres. Hemispheric assignments were restricted to their valid
angular ranges (right hemisphere: $-0.5\pi < \theta < 0.5\pi$; left hemisphere: $0.5\pi < \theta < 1.5\pi$ with
sub-ranges shifted by π to account for mirror symmetry).

354 The CMF values from both hemispheres were aggregated within the grid cells. When
356 multiple vertices contributed to the same grid cell, their CMF values were averaged to yield
a single representative estimate. This procedure was carried out both in polar coordinates
358 (ρ, θ) and, after coordinate conversion, in Cartesian coordinates (x, y) . This enabled con-
sistent visualization of cortical magnification across the entire visual field. As a quality
360 check, we confirmed that nearly all grid points within the defined field of view were assigned
valid CMF values after merging, indicating successful reconstruction of complete visual-field
magnification maps.

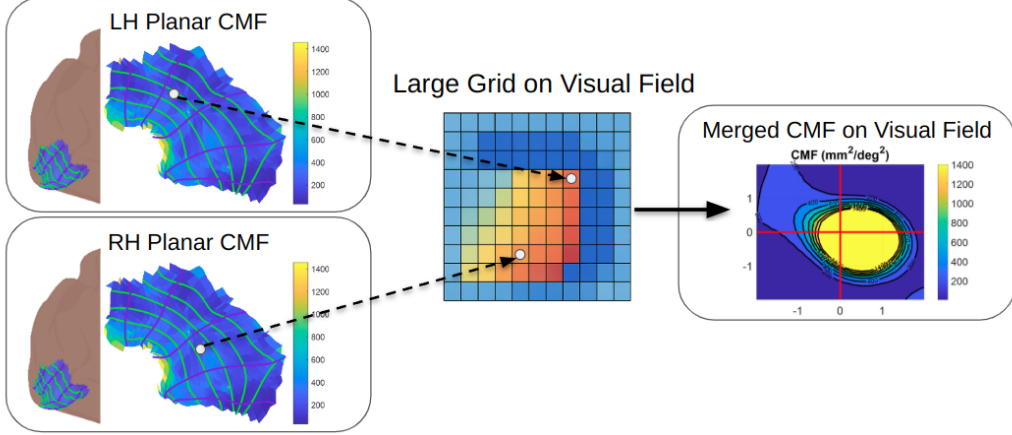


Figure 5: Illustration of the merging method: CMF results from left (LH) and right (RH) hemispheres are projected onto a common visual field grid and combined into a unified CMF representation.

This per-hemisphere merging procedure ensured that cortical magnification was computed consistently across subjects and that both hemispheres were seamlessly integrated into a unified, whole-field planar representation suitable for further group-level analysis.

3. Results

3.1. Optimal Transportation and Area Preserving

In our pipeline, optimal transport was used to compute an optimal area-preserving mapping between the original cortical surface and a parameterized planar disk. To evaluate its effectiveness, we conducted an ablation study on all 181 subjects in the HCP dataset. We quantified area distortion across all cortical mesh triangles during the transformation from the 3D brain structure to the 2D planar surface. The quality of this flattening—and its suitability for CMF measurements—was assessed by measuring the area distortion at each discrete triangle, comparing the original 3D mesh with the resulting flattened surface (Ta et al., 2022; Su et al., 2015b).

Conventional conformal mapping, which corresponds to smooth complex analytic functions, minimizes angle distortion but introduces significant area distortion. This trade-off undermines its suitability for 2D CMF measurements using area-based methods, such as the 1-ring patch approach. In contrast, integrating OT into the mapping process substantially

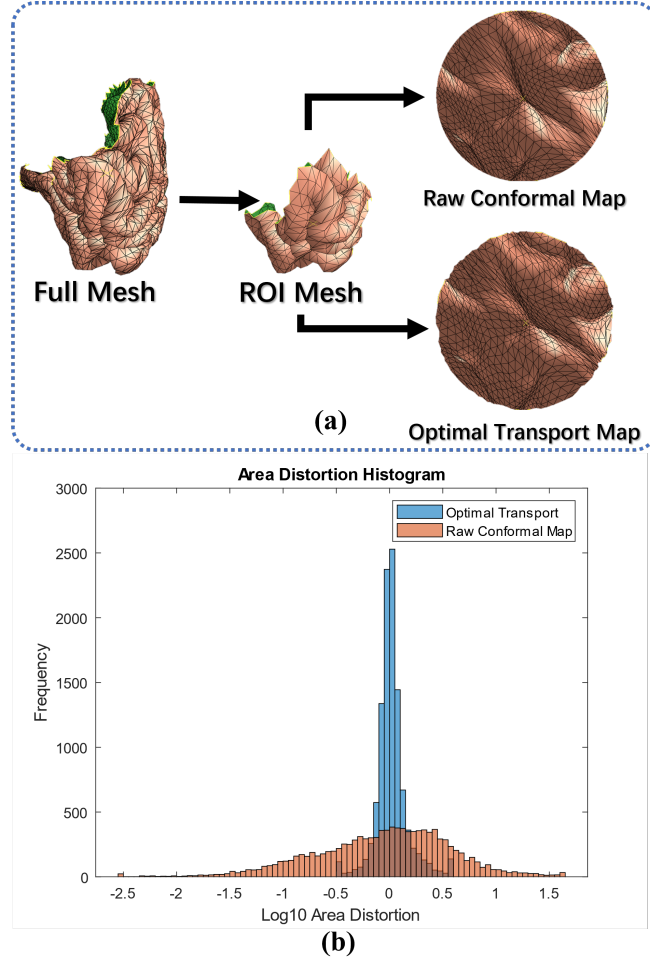


Figure 6: (a) Comparison of raw conformal mapping and optimal transport mapping from 3D brain mesh to 2D unit disk. (b) Comparison of area distortion between these 2 methods.

378 reduced area distortion.

As shown in Fig. 6, the incorporation of OT drastically reduced area distortion across the
 380 cortical mesh, approaching near-zero values, particularly within regions of interest (ROI).
 This enhanced area preservation enables more accurate CMF estimation through the 1-ring
 382 patch method, which relies on precision area measurements between the visual field and the
 cortical surface.

384 *3.2. CMF from the HCP Dataset*

The retinotopy data from all 181 healthy participants in the Human Connectome Project
 386 (HCP)(Benson et al., 2018a) where high quality 7T retinotopy data was acquired, were
 processed in this study using the proposed pipeline. After preprocessing of the entire early

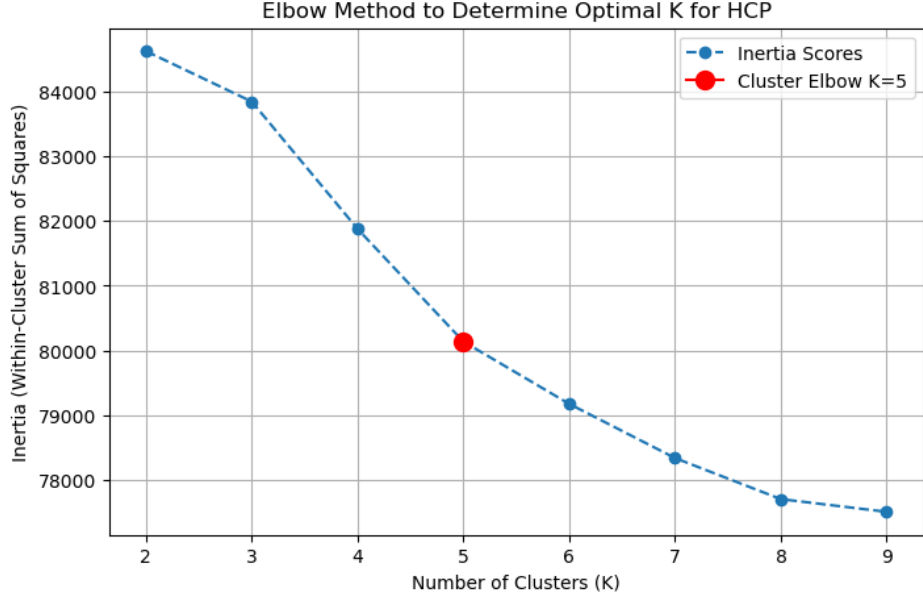


Figure 7: Elbow plot for K-means clustering of HCP CMF results. The plot shows the inertia (within-cluster sum of squares) as a function of the number of clusters. The optimal number of clusters, identified at the elbow point, is $K = 5$ when aggregating CMF data from all 181 HCP subjects.

388 visual cortex, we measure CMF solely on V1 and reported the results as follows.

3.2.1. CMF Results and Individual Differences

390 To analyze individual differences in CMF patterns across subjects, we applied K-means
 clustering to the CMF maps derived from the 181 observers in the HCP dataset. Specifically,
 392 the raw 2D matrices of CMF values in visual-field coordinates were used directly as input
 to the clustering, without additional feature extraction or dimensionality reduction (e.g.,
 394 PCA). The optimal number of clusters was determined to be $K = 5$, as indicated by the
 396 elbow point in the loss function curve (Fig. 7), reflecting the most significant reduction in
 398 loss without overfitting. To ensure robustness, the clustering procedure was repeated across
 multiple random initializations, and the resulting solutions consistently converged to similar
 cluster assignments.

This clustering allowed us to categorize subjects into groups with similar CMF profiles,
 400 revealing distinct patterns of visual information processing throughout the population. The
 average 2D planar CMF results for each cluster are shown in Fig. 8.

402 In all subjects, the CMF center was predominantly located near the foveal region, con-

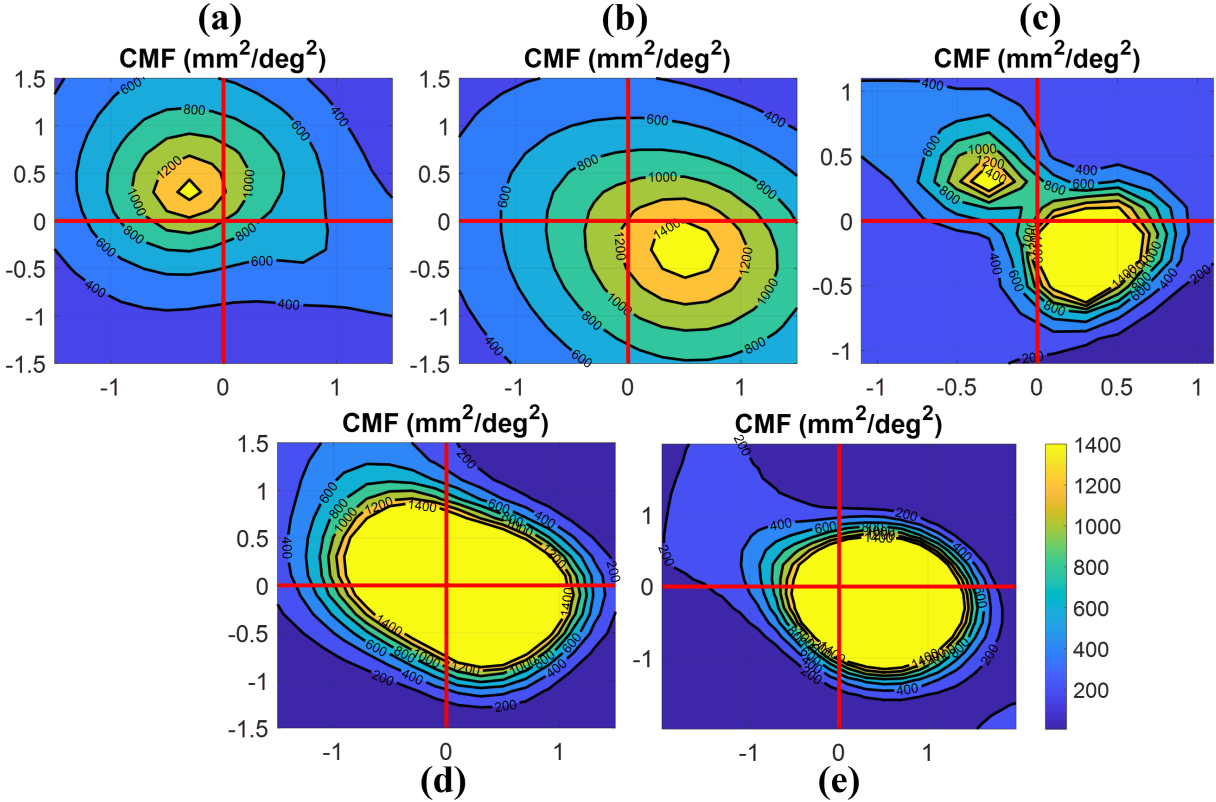


Figure 8: Average 2D planar V1 CMF results for 5 different clusters in the HCP cohort: (a) Upper-Left Cluster, CMF concentrated on the upper-left of the fovea in the visual field. (b) Lower-Right Cluster, CMF concentrated on the lower-right of the fovea. (c) Dual-Centralized Cluster, CMF held two concentration points on the upper-left and lower-right, respectively. (d) Centralized Cluster, CMF generally concentrates on the center of the fovea. (e) Lower-Centralized Cluster, CMF concentrates on the center with a slight offset to the bottom.

sistent with previous findings (Benson et al., 2021; Himmelberg et al., 2021; Harvey and Dumoulin, 2011; Silva et al., 2018; Kupers et al., 2022; Himmelberg et al., 2022). Besides, our estimated CMF magnitudes were consistent in scale with previous reports based on linear magnification measurements (Schira et al., 2009; Silva et al., 2018; Kupers et al., 2022), after accounting for the areal-to-linear conversion. Slight differences mainly reflect methodological factors, as our 1-ring areal computation averages across neighboring vertices, producing smoother estimates with smaller peaks near the fovea and higher values at larger eccentricities.

Furthermore, our clustering analysis revealed clear inter-subject variability in CMF asym-

Table 2: Number of observers for each cluster in the HCP cohort.

Clusters	# of observers
a. upper-left	32
b. lower-right	26
c. dual-centralized	11
d. centralized	47
e. lower-centralized	68

metry and concentration behavior, especially along the polar angle dimension. Table 2 summarizes the number of subjects assigned to each cluster. Most of the participants (115 of 181) fell into the centralized (47 subjects) or lower centralized (68 subjects) clusters, exhibiting a broad concentration of CMF that declined radially outward from the fovea. Despite this similarity, the two clusters differed in symmetry: the lower-centralized group showed a downward asymmetry, while the centralized group displayed a more symmetric distribution.

The remaining 66 subjects showed more localized and quadrant-specific patterns. Of these, 32 exhibited CMF concentration in the upper-left quadrant (Fig. 8b), and 11 subjects showed a dual centralized configuration with two distinct focal points (Fig. 8c), suggesting an unusual but consistent bilateral pattern.

To the best of our knowledge, no previous studies have systematically characterized this level of individual variability in CMF concentration behavior across the visual field. By categorizing participants into five distinct CMF profiles, our findings provide novel insights into how individuals may differ in their visual field processing. These differences, which are difficult to articulate through verbal descriptions alone, underscore the need for more research into the neural and functional implications of this diversity of the CMF.

3.2.2. Correlation between CMF and Receptive Field Size

In this study, we also examined the characteristics of pRF sizes across the visual field. Our results were consistent with previous literature (Adams and Horton, 2003; Van Essen et al., 1984; Harvey and Dumoulin, 2011; Hubel and Wiesel, 1974; Silva et al., 2018; Kupers et al., 2022) and revealed asymmetries in pRF size with respect to polar angle that aligned with

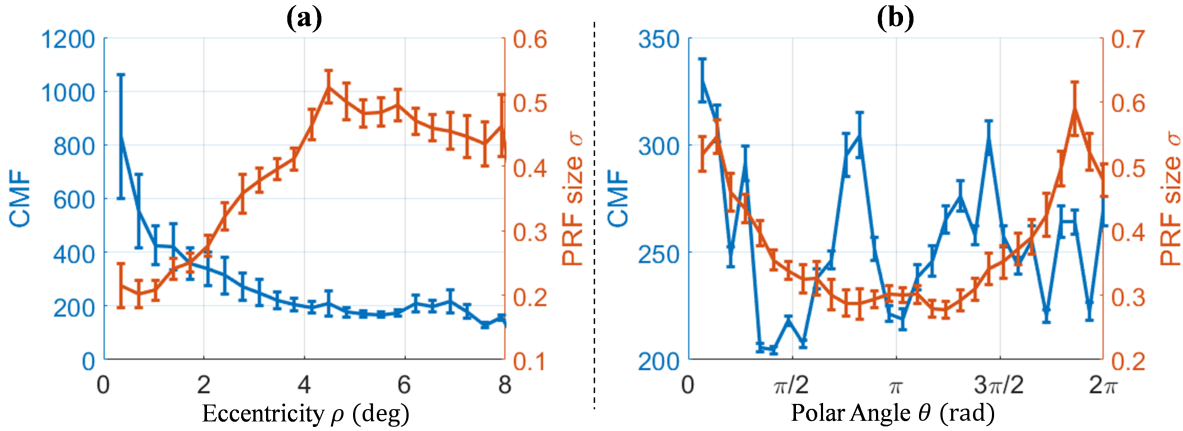


Figure 9: Correlation between CMF and pRF size across (a) eccentricity ρ and (b) polar angle θ

the results of our planar CMF measurements. Specifically, we found a negative correlation
 434 between the pRF size σ and CMF: as points moved outwards from the fovea (i.e., with
 increasing eccentricity), the pRF size σ increased while the CMF decreased (Fig. 9a). We
 436 also observed that pRF size σ and CMF were evenly distributed across different polar angles
 (Fig. 9b). These findings align with prior studies (Benson et al., 2021; Silva et al., 2018;
 438 Kupers et al., 2022; Himmelberg et al., 2022), which report that visual acuity is highest near
 the fovea and declines with eccentricity.

440 To provide quantitative support for these observations, we computed Pearson correlation
 coefficients and associated p-values across the 181 HCP subjects. The results are summarized
 442 in Table 3. A strong positive correlation was observed between pRF size and eccentricity,
 while CMF showed a strong negative correlation with eccentricity. Importantly, pRF size
 444 and CMF were negatively correlated, confirming the inverse relationship between these two
 measures.

Table 3: Quantitative correlations between pRF size, CMF, and eccentricity across HCP subjects.

Variables	Pearson R	p -value
pRF size vs. Eccentricity	0.749	1.643×10^{-5}
CMF vs. Eccentricity	-0.770	6.821×10^{-6}
pRF size vs. CMF	-0.695	1.140×10^{-4}

446 It has been widely accepted that pRF size and CMF exhibit a negative correlation across

variables such as eccentricity and polar angle (Harvey and Dumoulin, 2011). However,
448 our methodology allowed for a novel approach by projecting decoded pRF results directly
onto the 2D visual field, enabling precise calculation and visualization of planar CMF. This
450 projection made it possible to directly examine the correlation between pRF responses and
CMF within the 2D planar visual domain.

452 In addition to characterizing CMF patterns, we analyzed pRF solutions across all ob-
servers, as illustrated in Fig. 10. Notably, the inverse of the pRF size $1/\sigma$ was found to
454 closely align with our planar CMF measurements, further supporting the negative relation-
ship between pRF size and cortical magnification in the visual field.

456 It is well established that smaller pRF sizes or larger CMF values indicate higher visual
acuity near a given point, while acuity tends to decrease with increasing eccentricity. Con-
458 sequently, regions farther from the fovea usually exhibit larger pRF sizes and smaller CMF
values. In our study, we extended this understanding by analyzing the behavior of the pRF
460 size in planar coordinates, finding that pRF size not only increased with eccentricity but
also varied systematically with polar angle.

462 Furthermore, we observed that, for most subjects, the inverse of the pRF size $1/\sigma$
closely aligned with their CMF-based cluster. For instance, subject 905147 displayed a
464 dual-centralized pattern in both their planar CMF map and their $1/\sigma$ distribution. This
consistency between CMF and pRF measurements supports the validity of our clustering
466 approach and reinforces the assumed correlation between the two metrics.

Collectively, these findings demonstrate that individual differences in visual field repre-
468 sentation can be robustly characterized using both CMF and pRF analyses, offering com-
plementary insights into perceptual variability across subjects. The addition of quantitative
470 correlation metrics strengthens the evidence for the negative relationship between pRF size
and CMF.

472 *3.2.3. CMF Asymmetries*

In this study, we measured the planar CMF for all 181 observers in the HCP cohort on
474 their V1 cortex. Consistent with previous research (Adams and Horton, 2003; Van Essen
et al., 1984; Harvey and Dumoulin, 2011; Hubel and Wiesel, 1974; Silva et al., 2018; Kupers

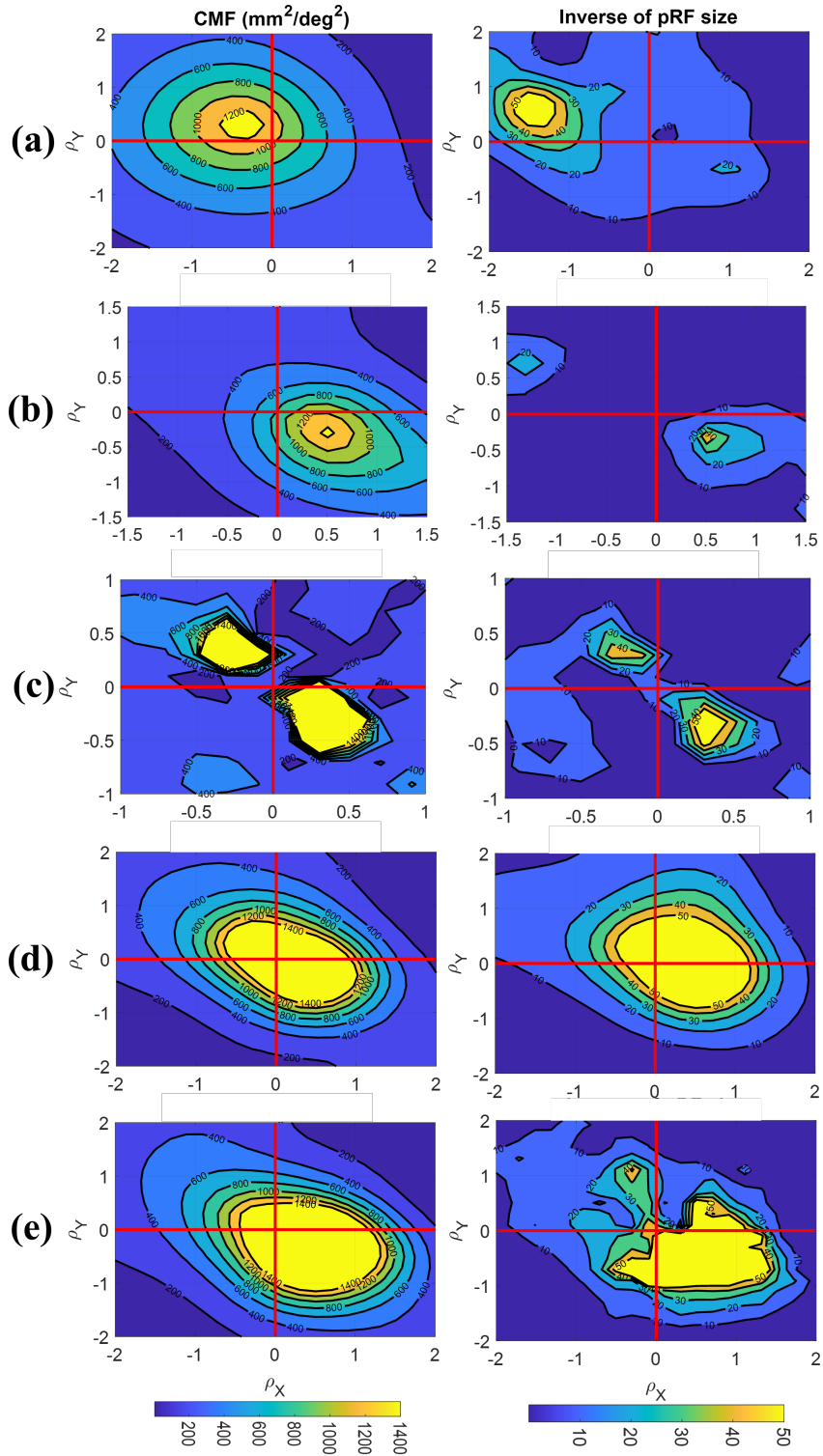


Figure 10: Example comparisons of planar CMF and the inverse of pRF size, $1/\sigma$: (a) subject 104416 (upper-left), (b) subject 114823 (lower-right), (c) subject 905147 (dual-centralized), (d) subject 146129 (centralized), and (e) subject 126426 (lower-centralized).

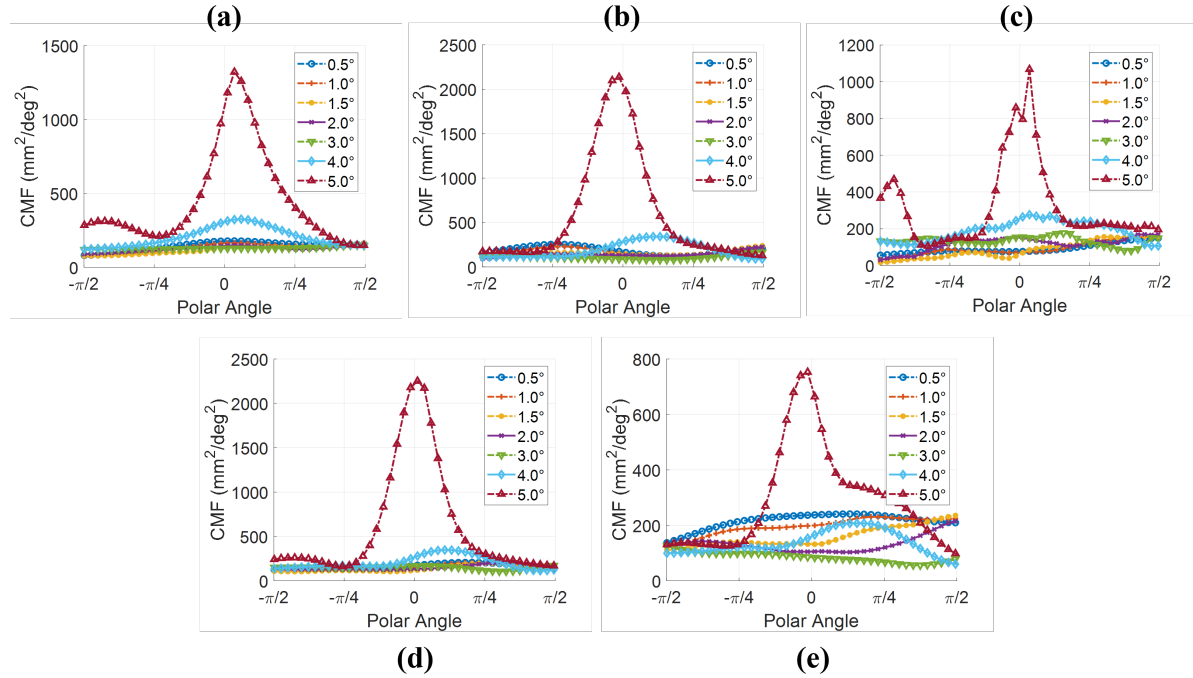


Figure 11: Examples of visual asymmetry in CMF as a function of polar angle across several eccentricities: (a) subject 104416 (upper-left), (b) subject 114823 (lower-right), (c) subject 905147 (dual-centralized), (d) subject 146129 (centralized), and (e) subject 126426 (lower-centralized)

et al., 2022), our observations revealed asymmetric visual field representations near the fovea. Specifically, some individuals exhibited increased CMF in the upper visual field, while others showed stronger representation in the lower visual field. Our planar CMF clustering analysis captured these individual differences, revealing distinct CMF behaviors around the fovea region.

Unlike previous approaches that assessed asymmetry by comparing broad horizontal (left vs. right) or vertical (upper vs. lower) quadrants (Silva et al., 2018; Harvey and Dumoulin, 2011), our method used planar CMF maps in two dimensions, incorporating both eccentricity and polar angle. This enabled a more nuanced assessment of visual field organization, revealing subject-specific asymmetry patterns near the fovea (Fig. 11). For example, observers with dominant CMF concentration in the upper-left versus lower-right visual field exhibited opposing asymmetry patterns, whereas those with a centralized CMF distribution displayed near-radial symmetry around the fovea.

In summary, our findings confirmed that early human visual field representations—especially

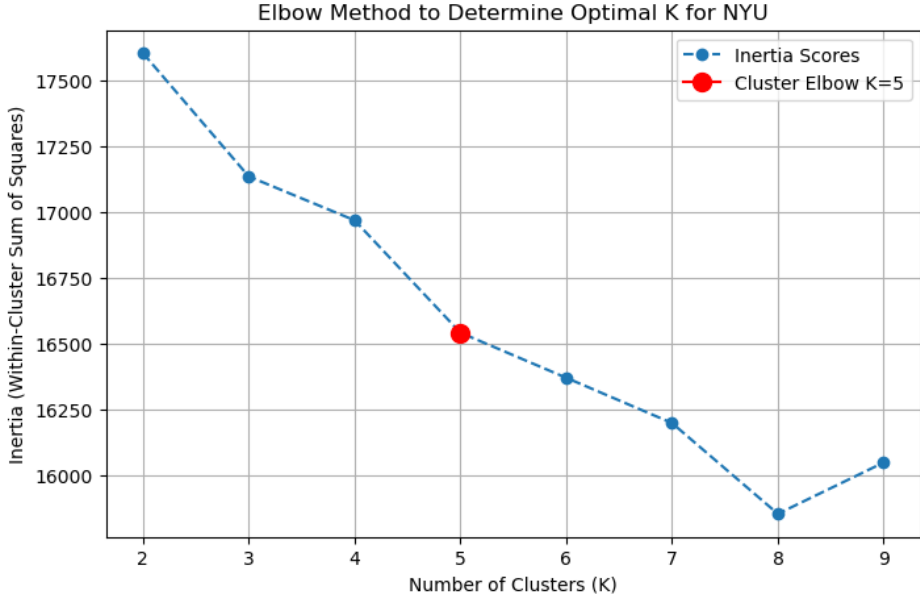


Figure 12: Elbow plot for K-means clustering of NYU CMF results. The plot shows the inertia (within-cluster sum of squares) as a function of the number of clusters. The optimal number of clusters, identified at the elbow point, is $K = 5$ when aggregating CMF data from all 42 NYU subjects.

in areas V1—were not radially symmetrical in terms of either CMF or pRF size. While the inverse relationship between pRF size and CMF with increasing eccentricity was consistent with classical models (Hubel and Wiesel, 1974), our results revealed that the location and extent of CMF asymmetry can vary considerably across individuals (Harvey and Dumoulin, 2011). This analysis provided a more nuanced understanding of individual differences in visual perception, highlighting the role of radial asymmetries in early visual processing.

3.3. CMF Validation Using the NYU Retinotopy Dataset

After analyzing CMF measurements from 181 observers in the HCP dataset, it was essential to validate our findings using an independent dataset with different experimental parameters and participant demographics. This step was critical in ensuring the robustness and generalizability of our observations on CMF asymmetries and clustering patterns. Although the HCP dataset offered high-resolution data acquired under specialized conditions, including 7T MRI scanners, long-duration scans, and a large cohort, it also reflected a unique experimental design. Validating our findings with alternative datasets helps control for possible biases or artifacts related to the HCP’s specific protocol.

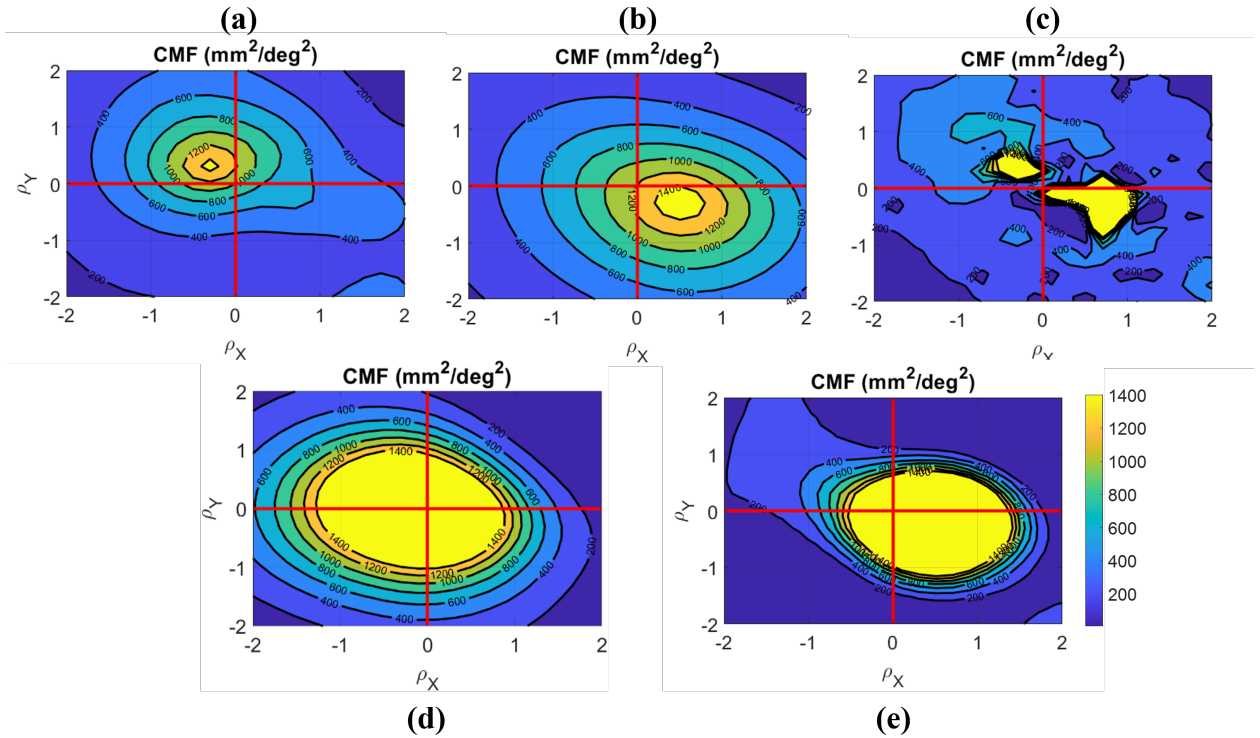


Figure 13: Average CMF results for all 5 clusters from the NYU dataset.

Recent studies (Himmelberg et al., 2021; Allen et al., 2022; Gong et al., 2023) have shown
 506 strong agreement with HCP on key retinotopic properties, despite differing setups. Thus,
 these independent datasets serve as important benchmarks for testing the reproducibility of
 508 retinotopic mapping and CMF estimation. In particular, they offer variability in scanner
 strength, task design, and subject cohorts, factors essential to confirm whether our CMF-
 510 based clustering and asymmetry findings are independent of the data set.

Among the available alternatives, we selected the New York University (NYU) Retinotopy
 512 Dataset (Ugurbil et al., 2013; Himmelberg et al., 2021), which includes a relatively large
 sample (44 subjects)—more than other public datasets (Allen et al., 2022; Gong et al.,
 514 2023)—making it a suitable cohort to validate the consistency of the behavioral clusters of
 CMF.

We applied our CMF estimation pipeline to 42 of the 44 NYU subjects and performed
 516 K-means clustering on the resulting CMF maps. Fig. 12 illustrates the inertia (within-
 cluster sum of squares) as a function of the number of clusters. The optimal number of
 518

clusters, identified at the elbow point, is $K = 5$ when aggregating the CMF data from the 520 42 subjects of NYU. Fig. 13 further shows the average CMF results of the five groups. They were consistent with those identified in the HCP dataset. Table 4 summarizes the number 522 of subjects in each NYU cluster, highlighting the persistence of CMF patterns in different datasets.

Table 4: Number of subjects for each cluster in the NYU retinotopy dataset.

Clusters	# of subjects in NYU 3T Dataset
a. upper-left	8
b. lower-right	14
c. dual-centralized	12
d. centralized	2
e. lower-centralized	6

524 This cross-dataset validation reinforced the reliability of our CMF estimation and clustering methods. The recurrence of consistent CMF behavior patterns across both high-field 526 (HCP) and standard-field (NYU) datasets confirmed that our findings were not artifacts of a specific imaging protocol or participant group. These results support the broad applicability 528 of our methods to various visual neuroscience studies and strengthen the case for using CMF-based analysis to capture meaningful individual differences in early visual cortex 530 organization.

4. Discussion

532 4.1. Limitations of Traditional CMF Quantification

Current methods for quantifying the Cortical Magnification Factor (CMF) exhibit several 534 limitations. Despite their widespread adoption (Horton and Hoyt, 1991; Virsu and Hari, 1996; Duncan and Boynton, 2003; Song et al., 2015; Hussain et al., 2015; Bordier et al., 536 2015; Lage-Castellanos et al., 2020; Benson et al., 2021; Himmelberg et al., 2021, 2023b), conventional approaches often lack precision and scalability. Key challenges include:

- 538 • Manual ROI Definition: Many studies rely on hand-drawn contours for defining regions
of interest (ROIs), which is time-consuming, lacks standardized criteria, and impairs
540 reproducibility.
- 542 • 1D CMF Measures: Most methods compute CMF linearly along eccentricity axes,
neglecting the inherently 2D nature of retinotopic representation.
- 544 • Geometric Inaccuracies: Existing projection techniques (e.g., graph distances, ortho-
graphic projections) distort the geometry of cortical surfaces and do not preserve topo-
logical continuity.

546 These limitations can introduce distortions in cortical area estimation, reduce measure-
ment accuracy, and impair continuity across the visual field, ultimately hampering a com-
548 prehensive understanding of cortical magnification.

4.2. Advancing CMF Estimation with Optimal Transport

550 To address these issues, we introduced an optimal transport (OT) framework for area-
preserving cortical surface parameterization (Su et al., 2015b). Building on quasiconfor-
552 mal geometry, our method incorporates the Beltrami coefficient (BC) to enforce topology-
preserving and smooth mappings (Tu et al., 2021). This framework supports the accurate
554 computation of 2D areal CMF using area ratios of 1-ring patches and can extend to multiple
visual areas (V1, V2, V3) through linear transformations of polar angle maps.

556 Our topology-preserving smoothing and OT-based parameterization significantly im-
proved retinotopic mapping. The BC helped maintain continuity and minimize distortion,
558 while additional phase correction steps resolved artifacts such as phase jumps. Together,
these components facilitated precise localization of the receptive field, enabling robust pla-
560 nar CMF measurements.

562 We validated our method on both 7T HCP (181 subjects) and 3T NYU (44 subjects)
datasets, demonstrating that our pipeline yielded consistent and reliable CMF estimates
under varying experimental conditions. This highlights the potential of our framework as a
564 versatile tool for retinotopic mapping in both research and clinical settings.

Table 5: Comparison of parameterization methods before CMF measurement

Methods	# of abnormal CMF points
1. Conformal Mapping + Topology smoothing	267
2. Proposed (OT + Topology smoothing)	89

4.3. Individual Differences in CMF

566 Previous studies have reported perceptual asymmetries in cortical magnification, such as
 567 horizontal-vertical asymmetry (HVA)(Schwarzkopf and Rees, 2013). These findings suggest
 568 that CMF is not a uniform function of eccentricity but reflects individual visual preferences
 569 and performance biases, reinforcing the need for personalized retinotopic analysis in both
 570 basic and translational research.

4.4. Impact of Optimal Transport

572 While conformal mapping methods (Tu et al., 2021; Ta et al., 2022; Tu et al., 2022a) have
 573 previously succeeded in preserving angular information and smoothing retinotopic maps,
 574 they proved insufficient for accurate CMF evaluation. Specifically, we observed that the
 575 application of topology smoothing alone could generate abnormal CMF values near the
 576 fovea due to overlapping or degenerate vertex rings. To mitigate this, we introduced optimal
 577 transport-based re-parameterization, which recalibrated visual coordinates and improved
 578 vertex spacing. As shown in Table 5, this adjustment reduced abnormal CMF points by over
 579 66 percent, making the data suitable for downstream tasks such as clustering.

580 4.5. Limitations and Future Directions

581 While our approach benefited from the high resolution and field strength of the 7T
 582 HCP dataset, limitations remained due to the inherent spatial resolution and signal-to-noise
 583 constraints in retinotopic imaging (Benson et al., 2018a).

584 Our study focused on the early visual areas and extending this work to higher-level visual
 585 areas (e.g., V4, MT) poses challenges due to reduced signal strength and increased variability
 586 in these regions. Additionally, clinical applications represent a promising future direction.
 587 Applying our framework to populations with visual disorders could improve understanding
 588 of functional reorganization and guide interventions for vision rehabilitation.

5. Conclusion

590 We developed a novel framework that integrates optimal transport and topological smoothing for accurate, area-preserving retinotopic mapping and 2D planar CMF estimation. Our
592 method corrects topological violations and enhances the precision of CMF quantification, enabling robust comparisons between subjects and datasets.

594 Applying this framework to 181 HCP 7T and 44 NYU 3T observers, we found that most
596 subjects had fovea-centered CMF profiles, but with significant individual differences in asym-
598 metry and spatial concentration. K-means clustering identified five distinct CMF behavioral
patterns—upper-left, lower-right, centralized, lower-centralized, and dual-centralized—which
were consistently observed across both datasets.

600 In addition, we found a strong negative correlation between CMF and pRF size, in
602 accordance with previous literature. The spatial distribution of $1/\sigma$ pRF estimates mirrored
the CMF profiles, further validating our approach.

604 In summary, this framework offers a powerful tool for precise, scalable, and biologically
faithful retinotopic analysis. Its application to clinical-grade fMRI data has the potential
to advance visual neuroscience and inform diagnostic and rehabilitative strategies for vision
disorders that affect billions worldwide.

606 6. Data and Code Availability

608 The data used in this research are publicly available and can be found in Benson et al.
610 (2018a). The code for processing the data and the experiment pipeline will be available upon
request or Github/Planar-CMF.

612 7. Acknowledgment

614 This work was partially supported by the National Science Foundation, United States
(DMS-1413417 and DMS-1412722) and the National Eye Institute, United States (R01EY032125).

8. Declaration of Interests

616 YX, ZL, and YW have a joint patent application “Xiong, Y., Z.-L. Lu, and Y. Wang, Sys-
618 tems and Methods for Planar Cortical Magnification Measurement”, under New York Uni-

616 vesity and Arizona State University (US patent application number PCT/US2024/014617).

9. Ethics Statement

618 This study was conducted using only publicly available and previously published datasets.
All data were originally collected in accordance with the ethical guidelines and institu-
620 tional review board (IRB) approvals of the respective research institutions responsible for
the datasets. No new data collection or participant recruitment was performed by the au-
622 thors. The datasets used in this study, including those from the Human Connectome Project
(HCP) and the NYU retinotopy dataset, were accessed and analyzed in full compliance with
624 their data use agreements and terms of access.

References

- 626 Adams, D.L., Horton, J.C., 2003. A precise retinotopic map of primate striate cortex gener-
ated from the representation of angioscotomas. *The Journal of neuroscience : the official
628 journal of the Society for Neuroscience* 23, 3771–89.
- Allen, E.J., St-Yves, G., Wu, Y., Breedlove, J.L., Prince, J.S., Dowdle, L.T., Nau, M.,
630 Caron, B., Pestilli, F., Charest, I., et al., 2022. A massive 7t fmri dataset to bridge
cognitive neuroscience and artificial intelligence. *Nature neuroscience* 25, 116–126.
- 632 Benson, N.C., Jamison, K.W., Arcaro, M.J., Vu, A.T., Glasser, M.F., Coalson, T.S., Van
Essen, D.C., Yacoub, E., Ugurbil, K., Winawer, J., Kay, K., 2018a. The Human Con-
634 nectome Project 7 Tesla retinotopy dataset: Description and population receptive field
analysis. *J Vis* 18, 23.
- 636 Benson, N.C., Jamison, K.W., Arcaro, M.J., Vu, A.T., Glasser, M.F., Coalson, T.S., Van Es-
sen, D.C., Yacoub, E., Ugurbil, K., Winawer, J., et al., 2018b. The human connectome
638 project 7 tesla retinotopy dataset: Description and population receptive field analysis.
Journal of vision 18, 23–23.

- 640 Benson, N.C., Kupers, E.R., Barbot, A., Carrasco, M., Winawer, J., 2021. Cortical magnification
in human visual cortex parallels task performance around the visual field. *Elife* 10,
642 e67685.
- Benson, N.C., Winawer, J., 2018. Bayesian analysis of retinotopic maps. *elife* 7, e40224.
- 644 Bois, C., Ronan, L., Levita, L., Whalley, H.C., Giles, S., McIntosh, A.M., Fletcher, P.C.,
Owens, D.C., Johnstone, E.C., Lawrie, S.M., 2015. Cortical surface area differentiates
646 familial high risk individuals who go on to develop schizophrenia. *Biological psychiatry*
78, 413–420.
- 648 Bonnotte, N., 2013. From knothe's rearrangement to brenier's optimal transport map. *SIAM
Journal on Mathematical Analysis* 45, 64–87.
- 650 Bordier, C., Hupé, J.M., Dojat, M., 2015. Quantitative evaluation of fmri retinotopic maps,
from v1 to v4, for cognitive experiments. *Frontiers in human neuroscience* 9, 277.
- 652 Brewer, A.A., Barton, B., 2014. Visual cortex in aging and Alzheimer's disease: changes in
visual field maps and population receptive fields. *Frontiers in psychology* 5.
- 654 Brewer, A.A., Liu, J., Wade, A.R., Wandell, B.A., 2005. Visual field maps and stimulus
selectivity in human ventral occipital cortex. *Nature neuroscience* 8, 1102.
- 656 Cheng, W., Frei, O., van der Meer, D., Wang, Y., O'Connell, K.S., Chu, Y., Bahrami,
S., Shadrin, A.A., Alnæs, D., Hindley, G.F., et al., 2021. Genetic association between
658 schizophrenia and cortical brain surface area and thickness. *JAMA psychiatry* 78, 1020–
1030.
- 660 Cowey, A., 1964. Projection of the retina on to striate and prestriate cortex in the squirrel
monkey, *saimiri sciureus*. *Journal of Neurophysiology* 27, 366–393.
- 662 Cowey, A., Rolls, E., 1974. Human cortical magnification factor and its relation to visual
acuity. *Experimental Brain Research* 21, 447–454.
- 664 Daniel, P.M., Whitteridge, D., 1961. The representation of the visual field on the cerebral
cortex in monkeys. *The Journal of Physiology* 159, 203–221.

- 666 DeYoe, E.A., Carman, G.J., Bandettini, P., Glickman, S., Wieser, J., Cox, R., Miller, D.,
Neitz, J., 1996. Mapping striate and extrastriate visual areas in human cerebral cortex.
668 Proceedings of the National Academy of Sciences 93, 2382–2386.
- 670 Dougherty, R.F., Koch, V.M., Brewer, A.A., Fischer, B., Modersitzki, J., Wandell, B.A.,
2003. Visual field representations and locations of visual areas v1/2/3 in human visual
cortex. Journal of vision 3, 1–1.
- 672 Dumoulin, S.O., Wandell, B.A., 2008. Population receptive field estimates in human visual
cortex. Neuroimage 39, 647–660.
- 674 Duncan, R.O., Boynton, G.M., 2003. Cortical magnification within human primary visual
cortex correlates with acuity thresholds. Neuron 38, 659–671.
- 676 Ecker, C., Ginestet, C., Feng, Y., Johnston, P., Lombardo, M.V., Lai, M.C., Suckling,
J., Palaniyappan, L., Daly, E., Murphy, C.M., et al., 2013. Brain surface anatomy in
678 adults with autism: the relationship between surface area, cortical thickness, and autistic
symptoms. JAMA psychiatry 70, 59–70.
- 680 Eilers, P.H., 2003. A perfect smoother. Analytical Chemistry 75, 3631–3636.
- 682 Engel, S., Zhang, X., Wandell, B., 1997. Colour tuning in human visual cortex measured
with functional magnetic resonance imaging. Nature 388, 68–71.
- 684 Engel, S.A., Rumelhart, D.E., Wandell, B.A., Lee, A.T., Glover, G.H., Chichilnisky, E.J.,
Shadlen, M.N., 1994. FMRI of human visual cortex.
- 686 Garcia, D., 2010. Robust smoothing of gridded data in one and higher dimensions with
missing values. Computational Statistics & Data Analysis 54, 1167–1178.
- Gong, Z., Zhou, M., Dai, Y., Wen, Y., Liu, Y., Zhen, Z., 2023. A large-scale fmri dataset
688 for the visual processing of naturalistic scenes. Scientific Data 10, 559.
- 690 Gu, X., Luo, F., Sun, J., Yau, S.T.T., Others, Xianfeng Gu, F.L., al., E., Gu, X., Luo,
F., Sun, J., Yau, S.T.T., Others, 2016. Variational principles for Minkowski type prob-

- lems, discrete optimal transport, and discrete Monge-Ampere equations. *Asian Journal of Mathematics* 20, 383–398. 1302.5472.
- 692 Harvey, B.M., Dumoulin, S.O., 2011. The relationship between cortical magnification factor and population receptive field size in human visual cortex: constancies in cortical architecture. *Journal of Neuroscience* 31, 13604–13612.
- 694 Hazlett, H.C., Poe, M.D., Gerig, G., Styner, M., Chappell, C., Smith, R.G., Vachet, C., Piven, J., 2011. Early brain overgrowth in autism associated with an increase in cortical surface area before age 2 years. *Archives of general psychiatry* 68, 467–476.
- 698 Himmelberg, M.M., Kurzawski, J.W., Benson, N.C., Pelli, D.G., Carrasco, M., Winawer, J., 2021. Cross-dataset reproducibility of human retinotopic maps. *Neuroimage* 244, 118609.
- 700 Himmelberg, M.M., Tünçok, E., Gomez, J., Grill-Spector, K., Carrasco, M., Winawer, J., 2023a. Comparing retinotopic maps of children and adults reveals a late-stage change in how v1 samples the visual field. *Nature communications* 14, 1561.
- 704 Himmelberg, M.M., Winawer, J., Carrasco, M., 2022. Linking individual differences in human primary visual cortex to contrast sensitivity around the visual field. *bioRxiv* , 2021–10.
- 706 Himmelberg, M.M., Winawer, J., Carrasco, M., 2023b. Polar angle asymmetries in visual perception and neural architecture. *Trends in Neurosciences* 46, 445–458.
- 708 Horton, J.C., Hoyt, W.F., 1991. The representation of the visual field in human striate cortex: a revision of the classic Holmes map. *Archives of ophthalmology* 109, 816–824.
- 710 Hubel, D.H., Wiesel, T.N., 1974. Uniformity of monkey striate cortex: A parallel relationship between field size, scatter, and magnification factor. *Journal of Comparative Neurology* 158, 295–305.
- 712 Hussain, Z., Svensson, C.M., Besle, J., Webb, B.S., Barrett, B.T., McGraw, P.V., 2015. Estimation of cortical magnification from positional error in normally sighted and amblyopic subjects. *Journal of Vision* 15, 25–25.

- Kammen, A., Law, M., Tjan, B.S., Toga, A.W., Shi, Y., 2016. Automated retinofugal visual pathway reconstruction with multi-shell HARDI and FOD-based analysis. *Neuroimage* 125, 767–779.
- 718
- Kay, K.N., Winawer, J., Mezer, A., Wandell, B.A., 2013. Compressive spatial summation in human visual cortex. *Journal of neurophysiology* 110, 481–494.
- 720
- Kay, N., Benson, C., Jamison, K., Arcaro, M., Vu, A., Coalson, T., Essen, D.V., Yacoub, E., Ugurbil, K., Winawer, J., Kay, K., 2018. The HCP 7T Retinotopy Dataset.
- 722
- Kupers, E.R., Benson, N.C., Carrasco, M., Winawer, J., 2022. Asymmetries around the visual field: From retina to cortex to behavior. *PLoS computational biology* 18, e1009771.
- 724
- Lage-Castellanos, A., Valente, G., Senden, M., De Martino, F., 2020. Investigating the reliability of population receptive field size estimates using fmri. *Frontiers in neuroscience* 14, 825.
- 726
- 728
- Lerma-Usabiaga, G., Benson, N., Winawer, J., Wandell, B.A., 2020. A validation framework for neuroimaging software: The case of population receptive fields. *PLoS computational biology* 16, e1007924.
- 730
- Lerma-Usabiaga, G., Winawer, J., Wandell, B.A., 2021. Population receptive field shapes in early visual cortex are nearly circular. *Journal of Neuroscience* 41, 2420–2427.
- 732
- Mensen, V.T., Wierenga, L.M., van Dijk, S., Rijks, Y., Oranje, B., Mandl, R.C., Durston, S., 2017. Development of cortical thickness and surface area in autism spectrum disorder. *NeuroImage: Clinical* 13, 215–222.
- 734
- 736
- Merkel, C., Hopf, J.M., Schoenfeld, M.A., 2018. Spatial elongation of population receptive field profiles revealed by model-free f mri back-projection. *Human Brain Mapping* 39, 2472–2481.
- 738
- Merkel, C., Hopf, J.M., Schoenfeld, M.A., 2020. Modulating the global orientation bias of the visual system changes population receptive field elongations. *Human Brain Mapping* 41, 1765–1774.
- 740
- 742

- Michel, M.M., Chen, Y., Geisler, W.S., Seidemann, E., 2013. An illusion predicted by V1
744 population activity implicates cortical topography in shape perception. *Nature Neuroscience* 16, 1477–1483.
- Morland, A.B., Baseler, H.A., Hoffmann, M.B., Sharpe, L.T., Wandell, B.A., 2001. Abnor-
746 mal retinotopic representations in human visual cortex revealed by fMRI. *Acta Psychologica* 107, 229–247.
- Palaniyappan, L., Mallikarjun, P., Joseph, V., White, T.P., Liddle, P.F., 2011. Regional
750 contraction of brain surface area involves three large-scale networks in schizophrenia.
Schizophrenia research 129, 163–168.
- Qiu, A., Rosenau, B.J., Greenberg, A.S., Hurdal, M.K., Barta, P., Yantis, S., Miller, M.I.,
752 2006. Estimating linear cortical magnification in human primary visual cortex via dynamic
programming. *Neuroimage* 31, 125–138.
- Rimol, L.M., Nesvåg, R., Hagler Jr, D.J., Bergmann, Ø., Fennema-Notestine, C., Hartberg,
756 C.B., Haukvik, U.K., Lange, E., Pung, C.J., Server, A., et al., 2012. Cortical volume,
surface area, and thickness in schizophrenia and bipolar disorder. *Biological psychiatry*
758 71, 552–560.
- Schira, M.M., Tyler, C.W., Breakspear, M., Spehar, B., 2009. The foveal confluence in
760 human visual cortex. *Journal of Neuroscience* 29, 9050–9058.
- Schira, M.M., Wade, A.R., Tyler, C.W., 2007. Two-dimensional mapping of the central and
762 parafoveal visual field to human visual cortex. *Journal of neurophysiology* 97, 4284–4295.
- Schneider, W., Noll, D.C., Cohen, J.D., 1993. Functional topographic mapping of the cortical
764 ribbon in human vision with conventional MRI scanners. *Nature* 365, 150.
- Schwartz, E.L., 1977. Spatial mapping in the primate sensory projection: Analytic structure
766 and relevance to perception. *Biological Cybernetics* 25, 181–194.
- Schwartz, E.L., 1980. Computational anatomy and functional architecture of striate cortex:
768 A spatial mapping approach to perceptual coding. *Vision Research* 20, 645–669.

- Schwarzkopf, D.S., Rees, G., 2013. Subjective size perception depends on central visual
770 cortical magnification in human v1. *PloS one* 8, e60550.
- Schwarzkopf, D.S., Song, C., Rees, G., 2011. The surface area of human V1 predicts the
772 subjective experience of object size. *Nature Neuroscience* 14, 28–30.
- Sereno, M.I., Dale, A.M., Reppas, J.B., Kwong, K.K., Belliveau, J.W., Brady, T.J., Rosen,
774 B.R., Tootell, R.B., 1995. Borders of multiple visual areas in humans revealed by functional
magnetic resonance imaging. *Science* 268, 889–893.
- 776 Shi, J., Wang, Y., 2020. Hyperbolic Wasserstein Distance for Shape Indexing. *IEEE Transactions on Pattern Analysis and Machine Intelligence* 42, 1362–1376.
- 778 Silva, M.F., Brascamp, J.W., Ferreira, S., Castelo-Branco, M., Dumoulin, S.O., Harvey,
B.M., 2018. Radial asymmetries in population receptive field size and cortical magnifica-
780 tion factor in early visual cortex. *NeuroImage* 167, 41–52.
- Song, C., Sandberg, K., Rutiku, R., Kanai, R., 2022. Linking human behaviour to brain
782 structure: further challenges and possible solutions. *Nature Reviews Neuroscience* 23,
517–518.
- 784 Song, C., Schwarzkopf, D.S., Kanai, R., Rees, G., 2015. Neural population tuning links
visual cortical anatomy to human visual perception. *Neuron* 85, 641–656.
- 786 Su, Z., Wang, Y., Shi, R., Zeng, W., Sun, J., Luo, F., Gu, X., 2015a. Optimal mass transport
for shape matching and comparison. *IEEE Transactions on Pattern Analysis and Machine
788 Intelligence* 37, 2246–2259.
- Su, Z., Wang, Y., Shi, R., Zeng, W., Sun, J., Luo, F., Gu, X., 2015b. Optimal Mass Transport
790 for Shape Matching and Comparison, in: *IEEE Transactions on Pattern Analysis and
Machine Intelligence*, pp. 2246–2259.
- 792 Swindale, N.V., Shoham, D., Grinvald, A., Bonhoeffer, T., Hübener, M., 2000. Visual cortex
maps are optimized for uniform coverage. *Nature Neuroscience* 3, 822–826.

- 794 Ta, D., Shi, J., Barton, B., Brewer, A., Lu, Z.L., Wang, Y., 2014. Characterizing human
retinotopic mapping with conformal geometry: a preliminary study, in: Ourselin, S.,
796 Styner, M.A. (Eds.), Medical Imaging 2014: Image Processing, p. 90342A.
- 798 Ta, D., Tu, Y., Lu, Z.L., Wang, Y., 2022. Quantitative characterization of the human
retinotopic map based on quasiconformal mapping. *Medical Image Analysis* 75, 102230.
- 800 Tootell, R.B., Hadjikhani, N.K., Vanduffel, W., Liu, A.K., Mendola, J.D., Sereno, M.I., Dale,
802 A.M., 1998. Functional analysis of primary visual cortex (v1) in humans. *Proceedings of
the National Academy of Sciences* 95, 811–817.
- 804 Tootell, R.B., Reppas, J.B., Kwong, K.K., Malach, R., Born, R.T., Brady, T.J., Rosen, B.R.,
Belliveau, J.W., 1995. Functional analysis of human MT and related visual cortical areas
using magnetic resonance imaging. *Journal of Neuroscience* 15, 3215–3230.
- 806 Tu, Y., Li, X., Lu, Z.L., Wang, Y., 2022a. Diffeomorphic registration for retinotopic maps
of multiple visual regions. *Brain Struct Funct* 227, 1507–1522.
- 808 Tu, Y., Li, X., Lu, Z.L., Wang, Y., 2022b. Protocol for topology-preserving smoothing of
BOLD fMRI retinotopic maps of the human visual cortex. *STAR Protoc* 3, 101614.
- 810 Tu, Y., Mi, L., Zhang, W., Zhang, H., Zhang, J., Fan, Y., Goradia, D., Chen, K., Caselli,
R.J., Reiman, E.M., et al., 2020. Computing univariate neurodegenerative biomarkers
with volumetric optimal transportation: a pilot study. *Neuroinformatics* 18, 531–548.
- 812 Tu, Y., Ta, D., Lu, Z.L., Wang, Y., 2021. Topology-preserving smoothing of retinotopic
maps. *PLoS Comput Biol* 17, e1009216.
- 814 Ugurbil, K., Xu, J., Auerbach, E.J., Moeller, S., Vu, A.T., Duarte-Carvajalino, J.M., Lenglet,
C., Wu, X., Schmitter, S., de Moortele, P.F., Others, 2013. Pushing spatial and temporal
816 resolution for functional and diffusion MRI in the Human Connectome Project. *Neuroim-
age* 80, 80–104.
- 818 Van Essen, D.C., Newsome, W.T., Maunsell, J.H.R., 1984. The visual field representa-
tion in striate cortex of the macaque monkey: asymmetries, anisotropies, and individual
820 variability. *Vision research* 24, 429–448.

- Van Essen, D.C., Smith, J., Glasser, M.F., Elam, J., Donahue, C.J., Dierker, D.L., Reid,
822 E.K., Coalson, T., Harwell, J., 2017. The brain analysis library of spatial maps and atlases
(BALSA) database. *Neuroimage* 144, 270–274.
- 824 Van Essen, D.C., Smith, S.M., Barch, D.M., Behrens, T.E., Yacoub, E., Ugurbil, K., Con-
sortium, W.M.H., et al., 2013. The wu-minn human connectome project: an overview.
826 *Neuroimage* 80, 62–79.
- Villani, C., 2008. Optimal transport: old and new. volume 338. Springer Science & Business
828 Media.
- Virsu, V., Hari, R., 1996. Cortical magnification, scale invariance and visual ecology. *Vision*
830 *research* 36, 2971–2977.
- Vuoksimaa, E., Panizzon, M.S., Chen, C.H., Fiecas, M., Eyler, L.T., Fennema-Notestine,
832 C., Hagler, D.J., Fischl, B., Franz, C.E., Jak, A., et al., 2015. The genetic association
between neocortical volume and general cognitive ability is driven by global surface area
834 rather than thickness. *Cerebral cortex* 25, 2127–2137.
- Vuoksimaa, E., Panizzon, M.S., Chen, C.H., Fiecas, M., Eyler, L.T., Fennema-Notestine, C.,
836 Hagler Jr, D.J., Franz, C.E., Jak, A.J., Lyons, M.J., et al., 2016. Is bigger always better?
the importance of cortical configuration with respect to cognitive ability. *Neuroimage* 129,
838 356–366.
- Wandell, B.A., Dumoulin, S.O., Brewer, A.A., 2007. Visual field maps in human cortex.
840 *Neuron* 56, 366–383.
- Wandell, B.A., Winawer, J., 2011. Imaging retinotopic maps in the human brain. *Vision*
842 *Research* 51, 718–737.
- Warnking, J., Dojat, M., Guérin-Dugué, A., Delon-Martin, C., Olympieff, S., Richard, N.,
844 Chéhikian, A., Segebarth, C., 2002a. fmri retinotopic mapping—step by step. *NeuroImage*
17, 1665–1683.

- 846 Warnking, J., Dojat, M., Guérin-Dugué, A., Delon-Martin, C., Olympieff, S., Richard, N.,
Chéhikian, A., Segebarth, C., 2002b. fMRI Retinotopic Mapping—Step by Step. *NeuroImage* 17, 1665–1683.
- 848
- 850 Waz, S., Wang, Y., Lu, Z.L., 2025. qPRF: A system to accelerate population receptive field decoding. *Neuroimage* 306, 120994.
- 852 Yu, X., Lei, N., Wang, Y., Gu, X., 2017. Intrinsic 3D dynamic surface tracking based on dynamic Ricci flow and Teichmuller map, in: Proceedings of the IEEE International Conference on Computer Vision, pp. 5390–5398.
- 854 Zacharopoulos, G., Klingberg, T., Kadosh, R.C., 2020. Cortical surface area of the left frontal pole is associated with visuospatial working memory capacity. *Neuropsychologia* 143, 107486.
- 856
- 858 Zeidman, P., Silson, E.H., Schwarzkopf, D.S., Baker, C.I., Penny, W., 2018. Bayesian population receptive field modelling. *Neuroimage* 180, 173–187.